ASAR—Antenna Synthetic Aperture Radar Imaging

Caner Ozdemir, *Member, IEEE*, Rajan Bhalla, Luiz C. Trintinalia, and Hao Ling, *Senior Member, IEEE*

***Abstract*—The antenna synthetic aperture radar (ASAR) imaging concept is introduced. We present the ASAR imaging algorithm to pinpoint the locations of secondary scattering off a platform from antenna radiation data. It is shown that a three-dimensional (3-D) ASAR image of the platform can be formed by inverse Fourier transforming the multifrequency, multiaspect far-field radiation data from an antenna mounted on the platform. This concept is demonstrated using the computed radiation data from the code Apatch, which employs the shooting and bouncing ray (SBR) technique. Furthermore, we develop a fast ASAR algorithm specially tailored for the SBR approach. By taking advantage of the ray tracing information within the SBR engine, we demonstrate that the fast approach can result in the same quality of image as the frequency-aspect algorithm at only a fraction of the computation time.**

***Index Terms*— Antennas, electromagnetic scattering, feature extraction, radar cross section, SAR imaging.**

I. Introduction

IT IS well known that antenna characteristics can be dramatically altered by the platform that supports the antenna structure (Fig. 1). It is therefore important to study platform effects and explore ways to reduce or mitigate such effects. Recently, the advent of computational electromagnetics (CEM) algorithms has made the problem of characterizing antenna performance on highly complex platforms realizable. For instance, an exact numerical solution to Maxwell's equations is now possible for full-size aircraft up to a frequency of about 1 GHz [1], [2]. Furthermore, an approximate high-frequency solution based on the shooting and bouncing ray (SBR) method [3]–[6] is also available for frequencies up to 10 GHz and beyond. While these "forward" solution algorithms are a first step toward addressing the platform issue, an equally important problem is the "inverse" algorithm of spatially pinpointing where on the platform the undesirable scattering is coming from based on CEM data. Previously, a holographic diagnostic technique has been developed to map the surface distortion on reflector antennas from far-field radiation pattern [7], [8]. In this work, we set out to develop such a diagnostic algorithm to process CEM data for general antennas mounted on complex structures.

(a) (b)

Fig. 1. The radiation pattern of a stand-alone (a) antenna can be dramatically altered by the platform that supports the (b) antenna structure.

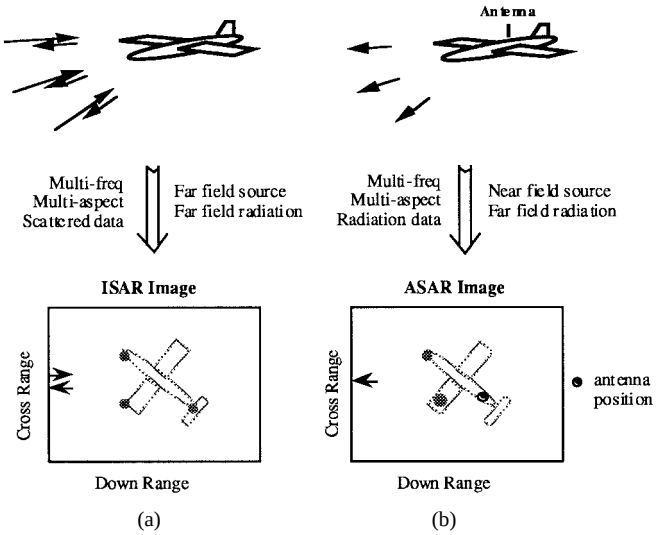

Fig. 2. (a) The conventional ISAR scenario. (b) The present ASAR scenario.

Our approach is based on the inverse synthetic aperture radar (ISAR) concept. ISAR imaging is a standard technique used in the microwave radar community to map the locations of dominant scattering off a target based on multifrequency, multiaspect backscattered data [9]. We shall extend this concept to the antenna radiation problem. By collecting multifrequency, multiaspect radiation data from an antenna mounted on a complex platform, we set out to generate an ASAR (i.e., antenna SAR) image of the platform that will allow us to pinpoint the dominant *secondary radiation* off the platform. Contrary to the conventional ISAR imaging, a key complication of the ASAR imaging scenario is that the antenna is located in the near field of the platform (Fig. 2).

In this paper, we first present the ASAR imaging algorithm. In Section II, it is shown that under the small-angle approximation and single-bounce assumption, a Fourier transform relationship exists between multifrequency, multiaspect radiation data and the three-dimensional (3-D) positions and strengths

Manuscript received December 12, 1996; revised September 11, 1998. This work was supported by the Air Force MURI Center for Computational Electromagnetics under Contract AFOSR F49620-96-1-0025, the Joint Services Electronics Program under Contract AFOSR F49620-95-C-0045, and DEMACO under Contract DEM-95-UTA-55.

C. Ozdemir was with the Department of Electrical and Computer Engineering, The University of Texas at Austin. He is now with Allied Signal, Columbia, MD USA.

R. Bhalla and H. Ling are with the Department of Electrical and Computer Engineering, University of Texas at Austin, Austin, TX 78712 USA.

L. C. Trintinalia is with the Department of Electronic Engineering, Escola Politecnica da Universidade, Sao Paulo, Brazil.

Publisher Item Identifier S 0018-926X(98)09690-2.

of the secondary scatterers on the platform. Therefore, a 3-D image showing the spatial locations of platform scattering can be constructed via Fourier inversion of the radiation data. We demonstrate this concept by using the computed radiation data from a mounted antenna on a model airplane, simulated using the SBR-based code Apatch [5], [6]. By forming the 3-D image using the ASAR algorithm, the key scattering locations on the platform can be clearly identified. In Section III, we further derive a fast ASAR imaging algorithm specially tailored for the SBR approach. By taking advantage of the ray tracing information within the SBR engine, we show that the ASAR image can be generated directly in the image domain without resorting to any multiple frequency-aspect calculations. Such idea is similar to the image-domain ISAR formation process we have reported previously [10]. Next, we further apply a fast Fourier transform (FFT)-based algorithm [11], [12] to speed up the ASAR image formation time. It will be shown that, using such a fast approach, we can obtain the same quality of image as the frequency-aspect algorithm at only a fraction of the computation time (minute versus hour). This result demonstrates that a fast computer design tool which combines antenna pattern simulation with scattering location diagnostic can be readily implemented to investigate platform effects.

II. ASAR Algorithm

A. Formulation

In this section, we shall derive the general ASAR imaging algorithm that utilizes multifrequency, multiaspect, far-field radiation data. Let us assume that an antenna is located at the origin as depicted in Fig. 3. In addition to the direct antenna radiation, we consider the secondary radiation from the antenna–platform interaction. If we assume the scattering comes from a single-point scatterer on the platform at a point $P(x_o, y_o, z_o)$, we can reason that the scattered field about the $-x$-direction is given by

$$E^s(\omega, \phi, \theta) = A \cdot e^{-jkr_o} \cdot e^{-jk(x_o \cos\theta \cos\phi + y_o \cos\theta \sin\phi + z_o \sin\theta)} \tag{1}$$

where A is the strength of the scattered signal, $r_o = \sqrt{x_o^2 + y_o^2 + z_o^2}$ is the path traveled by the radiated signal from the antenna to point P, and k is the free-space wavenumber. Note that the first exponential accounts for the phase lag from the antenna to point P, while the second exponential accounts for the additional phase lag from point P to the observation direction relative to the direct radiation from the antenna. Next, we utilize two assumptions commonly used in ISAR imaging, namely: 1) the observation angles θ and ϕ are small and 2) the radiation data are collected within a certain bandwidth that is small compared to the center frequency of operation. Combining these assumptions, we can approximate

$$\begin{aligned} k_x &= k \cos\theta \cos\phi \cong k \\ k_y &= k \cos\theta \sin\phi \cong k_o\phi \\ k_z &= k \sin\theta \cong k_o\theta \end{aligned} \tag{2}$$

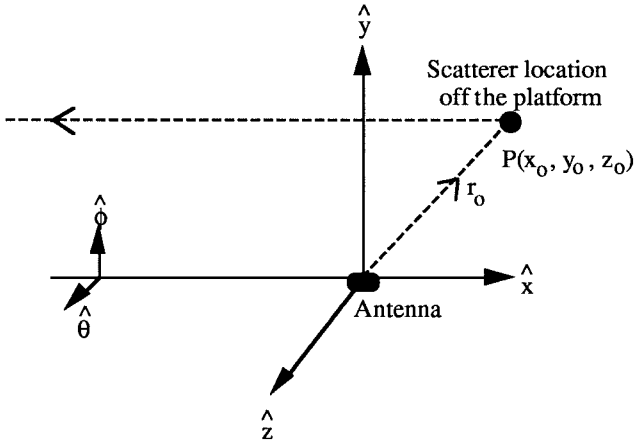

Fig. 3. The path of the radiated signal which is scattered off a point on the platform.

where k_o is the wavenumber at the center frequency. Substituting the above approximations into (1), we obtain the following equation for the scattered field:

$$E^s(\omega, \phi, \theta) \cong A \cdot e^{-jk(r_o + x_o)} \cdot e^{-jk_o\phi y_o} \cdot e^{-jk_o\theta z_o}. \tag{3}$$

In the above equation, it is obvious that there are Fourier transform relationships between k and $(r+x)$, $k_o\phi$ and y, and $k_o\theta$ and z, respectively. The idea behind the ASAR algorithm is that if we take the 3-D inverse Fourier transform (IFT) of the scattered field with respect to k, $k_o\phi$, and $k_o\theta$, it is possible to retrieve the location and strength of the point scatterer on the platform. Let us define a new variable $u = r + x$. Then the 3-D ASAR image is generated via

$$\begin{aligned} \text{ASAR}(u, y, z) &= \text{IFT}_3\{E^s(\omega, \phi, \theta)\} \\ &= \text{IFT}_3\left\{A \cdot e^{-jku_o} \cdot e^{-jk_o\phi y_o} \cdot e^{-jk_o\theta z_o}\right\} \\ &= A \cdot \delta(u - u_o) \cdot \delta(y - y_o) \cdot \delta(z - z_o). \end{aligned} \tag{4}$$

Therefore, by inverse Fourier transforming the multifrequency, multiaspect radiation data, the point scatterer will manifest itself as a peak in the ASAR image at (u_o, y_o, z_o) with amplitude A. In practice, the actual spot size of the peak will, of course, not be infinitesimal but will depend on the actual bandwidth of the data in frequency and angles.

Note that an additional complication exists as we have not yet constructed the ASAR image in the original (x, y, z) domain. A transformation is needed to bring the ASAR image from the (u, y, z) domain to the desired (x, y, z) domain. Since $u = r + x = \sqrt{x^2 + y^2 + z^2} + x$, when we solve for x in terms of u, we arrive at the following transformation formula:

$$x = \frac{1}{2}\left(u - \frac{(y^2 + z^2)}{u}\right). \tag{5}$$

The effect of the u-to-x transformation is depicted in Fig. 4. In Fig. 4(a), the uniform u–y grid for $z = 0$ is plotted. Since the transformation from u to x is not linear, the resulting x–y grid after the transformation is a nonuniform one, as shown in Fig. 4(b). The points $x > 0$ correspond to the region behind the antenna (i.e., away from the observation region of interest). In this region the grid is nearly uniform. However,

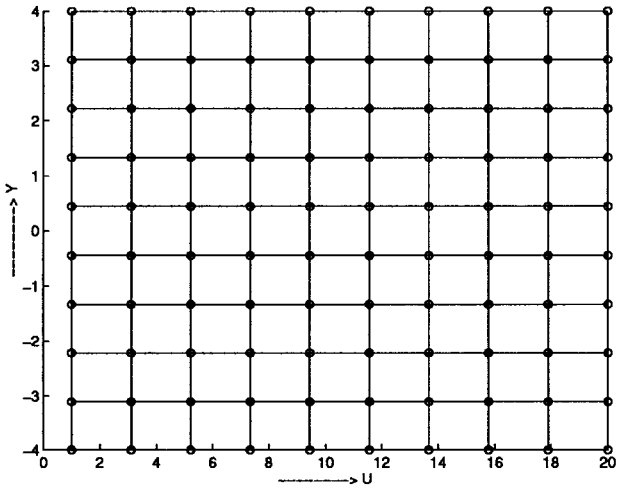

(a)

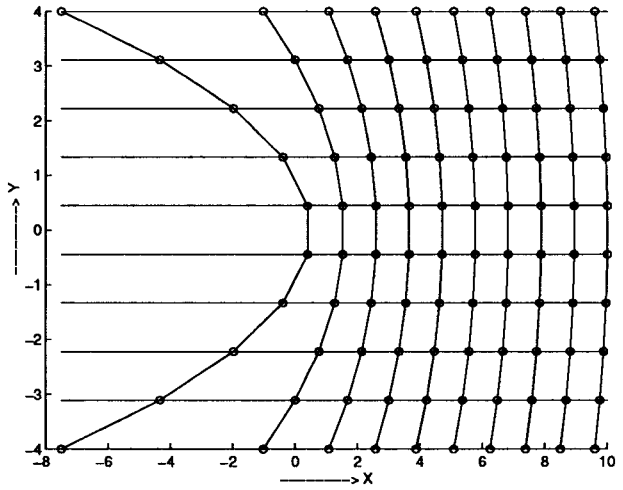

(b)

Fig. 4. An example showing the effect of the u-to-x transformation. (a) The uniform u–y grid for $z = 0$. (b) The corresponding (distorted) x–y grid.

the x–y grid becomes highly distorted for the $x < 0$ region which corresponds to the region in front of the antenna toward the observation direction. Therefore, as we will see in the resulting ASAR image in the examples, the platform scattering mechanisms from the region in front of the antenna will experience distortion due to such an u-to-x transformation.

To summarize, the general algorithm in ASAR imaging consists of three steps.

1) Collect multifrequency, multiaspect radiation field data $E^s(\omega, \phi, \theta)$.
2) Take the 3-D inverse Fourier transform of $E^s(\omega, \phi, \theta)$ to form ASAR(u, y, z).
3) Use the u-to-x transformation to generate ASAR(x, y, z).

The dominant scattering locations on the platform at the observation angles of interest should then be manifested as peaks in the resulting ASAR image. Before demonstrating this algorithm using examples, several remarks are in order. First, borrowing our terminology from ISAR imaging, we shall refer to the x-direction as the down range direction. The y- and z-axes are two orthogonal cross-range directions. From (3), we

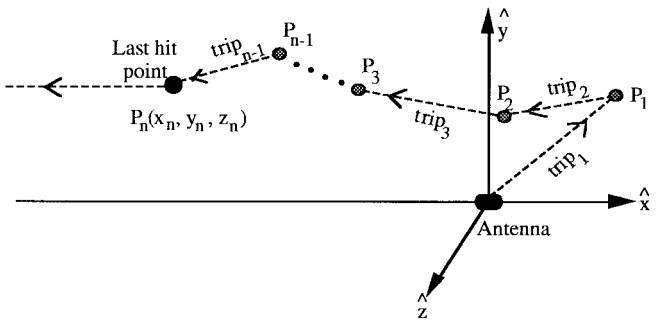

Fig. 5. The path of the radiated signal due to a multiple bounce mechanism.

can clearly see that the resolution in x comes from frequency diversity, while the resolutions in y and z come from angular diversity. However, since the ASAR concept is based on one-way radiation rather than the two-way backscattering scenario of ISAR imaging, it requires twice the bandwidth in frequency and angles to generate the same resolution as in an ISAR imagery. For instance, to achieve $6''$ of down range resolution requires 1 GHz of bandwidth in ISAR, but 2 GHz of bandwidth in ASAR. We should also note that this estimate assumes a uniform amplitude and linear phase behavior of the antenna frequency response. If the antenna frequency response deviates significantly from this assumption, the down-range resolution will be degraded. Second, contrary to ISAR, an additional u-to-x transformation is necessary to unwrap the nonlinear phase term arising from the propagation delay from the antenna to the point scatterer on the platform. This results in an additional image distortion which is most severe along the -x direction. Physically, this phenomenon can be explained by the fact that it is not possible to resolve point scatterers along the $-x$-axis as all these mechanisms have the same path length. Although the image distortion can be partially alleviated by oversampling in the u-domain, it cannot be completely circumvented. Third, the present ASAR algorithm, just like the ISAR algorithm, is based on a single-bounce assumption. Multiple-bounce mechanisms will not be correctly mapped in the ASAR image to the actual locations of the platform scattering. However, as we shall show next, a higher order scattering mechanism will simply be delayed in the down-range direction while along the two cross-range directions it will be mapped to the last bounce point on the platform.

To illustrate how multibounce mechanisms are represented in the ASAR image, we consider an n-bounce mechanism as depicted in Fig. 5. The corresponding scattered field is given by the equation

$$\begin{aligned} E^s(\omega, \phi, \theta) &= A \cdot e^{-jk(\{trip_1 + trip_2 + \cdots + trip_{n-1}\} + x_n)} \\ &\quad \cdot e^{-jk_o \phi y_n} \cdot e^{-jk_o \theta z_n} \\ &= A \cdot e^{-jk(trip_{total + x_n})} \cdot e^{-jk_o \phi y_n} \cdot e^{-jk_o \theta z_n}. \end{aligned} \tag{6}$$

By taking the 3-D inverse Fourier transform of the above signal, we obtain

$$\text{ASAR}(u, y, z) = A \cdot \delta(u - u'_n) \cdot \delta(y - y_n) \cdot \delta(z - z_n) \tag{7}$$

where $u'_n = \text{trip}_{\text{total}} + x_n$. Notice that the y- and z-coordinate of the *last* hit point are meaningfully represented in the ASAR

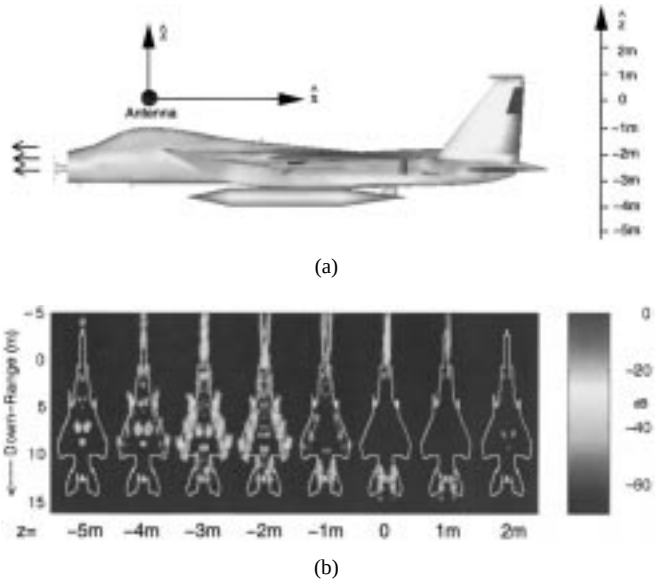

(a)

(b)

Fig. 6. (a) Side view of the "v1old" model. (b) The 3-D ASAR images for different z slices at nose-on.

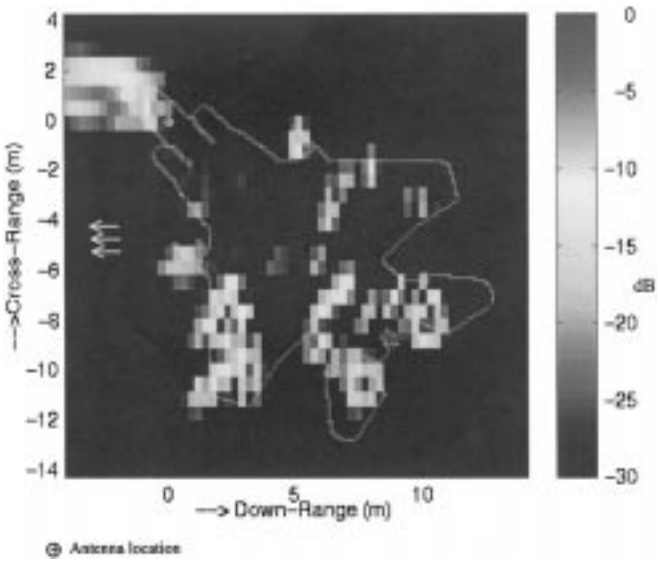

Fig. 7. The 2-D projected ASAR image at 45° from nose-on.

image. Next, we apply the u-to-x transformation to generate

$$\text{ASAR}(x, y, z) = A \cdot \delta(x - x'_n) \cdot \delta(y - y_n) \cdot \delta(z - z_n) \quad (8)$$

where

$$x'_n = \frac{1}{2}\left(u'_n - \frac{(y_n^2 + z_n^2)}{u'_n}\right). \quad (9)$$

Since u'_n is always greater than $u_n = \sqrt{x_n^2 + y_n^2 + z_n^2} + x_n$, this implies that x'_n will always be greater than x_n. In other words, the ASAR peak for a multibounce scattering feature will not be at the last bounce point, but rather will be simply delayed in the down-range direction by x'_n–x_n. Therefore, multiple bounce features in the ASAR image, if properly interpreted, do carry useful information for image understanding.

B. Numerical Examples

The ASAR imaging algorithm has been tested using the simulated radiation data from a dipole antenna placed next to simple plate configurations. The tests showed the expected specular peaks on the plate in the resulting images. These results will not be shown here for brevity. In the first example presented here, we generate the ASAR image using the simulated radiation data from an antenna mounted on a complex airplane model. The CAD model of the airplane, "v1old," consists of approximately 10 000 facets and is assumed to be perfectly conducting. The side view of the model is shown in Fig. 6(a). The CEM simulation is carried out by the SBR-based code Apatch. A dipole antenna whose length is electrically small $(\sim\lambda/10)$ is used as the source and placed above the cockpit. During the CEM simulation, a large set of rays are shot from the antenna toward to platform and are traced according to geometrical optics as they bounce around the platform. The density of rays cast on the platform is four rays per wavelength at the center frequency. At the exit point of each ray, a ray-tube integration is carried out to find the contribution of each ray to the total radiated field at various frequencies and observation angles [13]. The frequency bandwidth used is 1.1 GHz with a center frequency of 10 GHz. A total of 128 frequencies are computed within this band. The scattered field is collected in the far field from $-1.67°$ to $1.67°$ in azimuth over 32 points and from $-0.85°$ to $0.85°$ in elevation over eight points. Therefore, for each frequency point, we collect $32 \times 8 = 256$ angular points. In the computed data, we include only the scattered field from the platform and not the primary radiation due to the antenna in the absence of the platform. The total computation time for the CEM simulation is 80 h on an IBM RS6000/590 workstation. Next, a 3-D ASAR image is generated using the algorithm discussed earlier. A 3-D Hanning window is used prior to the inverse FFT operation in the algorithm. Since the ASAR image is 3-D, we present the ASAR image of "v1old" in the xy-plane for different z-cuts in Fig. 6(b). We observe a number of distinct point scatterers on the wings and the tail of the aircraft. Since the antenna is located near the cockpit, the strongest platform scattering is from the specular points around the nose of the aircraft. However, as we expect, this region is distorted due to the u-to-x transformation.

In the next example, we use the same airplane model, except the far-field data are collected from $-46.45°$ to $-43.55°$ in azimuth over 32 points and from $-0.85°$ to $0.85°$ in elevation over eight points. Again, the frequency bandwidth is 1.1 GHz with a total of 128 frequencies around the center frequency of 10 GHz. A 3-D Hanning window is used to reduce the sidelobes in the image. In this example, instead of showing all the individual z slices, we form a two-dimensional (2–D) projected ASAR image in the x–y plane by summing all the z-cuts, as shown in Fig. 7. By viewing the resulting 2-D ASAR image, the dominant scattering regions for this particular observation angle are found to be located on the left wing and around the tail fins of the aircraft. Again, we notice

the unavoidable image smearing in front of the antenna due to the u-to-x transformation.

III. Fast ASAR Image Formation Using SBR

We have thus far presented a general Fourier-based algorithm to generate 3-D ASAR imageries from multifrequency, multiaspect radiation data. For complex platforms, the computation time needed to generate the required input data set using a CEM simulator can become prohibitively high. In this section, we shall derive a fast imaging algorithm specially tailored for the SBR approach. It utilizes the ray information available within the ray-tracing engine to generate the ASAR image directly on a ray-by-ray basis. As we shall demonstrate, when we combine this image-domain formulation with a fast ray summation scheme, we can obtain the same quality of image as the frequency-aspect algorithm at only a fraction of the computation time. This approach is similar to the fast image formation algorithm we have successfully developed for ISAR image simulation [10], [12].

A. Image-Domain Formulation

In applying the SBR technique to the antenna radiation problem, rays are first shot from the phase center of the antenna and traced according to geometrical optics. At the exit point of each ray before they leave the platform altogether, a ray-tube integration is carried out to find the contribution of each ray to the total radiated field at various frequencies and observation angles [13]. Under this construct, the radiated field can be written as

$$E^s(\omega, \phi, \theta) = \sum_{i\,\text{rays}} \alpha_i \cdot e^{-jku_i} \cdot e^{-jk_o\phi y_i} \cdot e^{-jk_o\theta z_i}. \quad (10)$$

The above expression is derived under the assumption that the bandwidth and observation angles are small, and that the platform is perfectly conducting. The detailed steps can be found in [10] and will not be repeated here. In (10), α_i is proportional to the field at the exit ray-tube, and is only weakly dependent on aspect and frequency. (x_i, y_i, z_i) is the location of the last hit point and $u_i = d_i + x_i$, where d_i is the total path traveled by i'th ray from the antenna to the last hit point. Substituting (10) into our general ASAR formula, we obtain

$$\begin{aligned}&\text{ASAR}(u, y, z)\\ &\quad = \text{IFT}_3\{E^s(\omega, \phi, \theta)\}\\ &\quad = \text{IFT}_3\left\{\sum_{i\,\text{rays}} \alpha_i \cdot e^{-jku_i} \cdot e^{-jk_o\phi y_i} \cdot e^{-jk_o\theta z_i}\right\}\\ &\quad = \sum_{i\,\text{rays}} \alpha_i \cdot \text{IFT}\{e^{-jku_i}\} \cdot \text{IFT}\{e^{-jk_o\phi y_i}\} \cdot \text{IFT}\{e^{-jk_o\theta z_i}\}.\end{aligned} \quad (11)$$

It is apparent that the above inverse Fourier transform operations can be performed analytically, resulting in a closed-form expression for the ASAR image of the platform

$$\begin{aligned}&\text{ASAR}(u, y, z)\\ &\quad = \sum_{i\,\text{rays}} \alpha_i\{2\Delta k e^{jk_o(u-u_i)}\,\text{sinc}\,(\Delta k(u-u_i))\}\\ &\qquad \cdot \{2k_o\Delta\phi\,\text{sinc}\,(k_o\Delta\phi(y-y_i))\}\\ &\qquad \cdot \{2k_o\Delta\theta\,\text{sinc}\,(k_o\Delta\theta(z-z_i))\}\end{aligned} \quad (12)$$

where Δk, $\Delta\phi$, and $\Delta\theta$ are the half bandwidths in the k-, ϕ-, and θ-domain, respectively. Notice that this "image-domain" formula gives the contribution of each ray, in closed form, to the overall ASAR image directly. Since $(\alpha_i, u_i, y_i, z_i)$ are readily available from ray tracing, the ASAR image can be generated directly without first computing the multiple frequency-aspect data. Therefore, to form an ASAR image using (12), we simply update the (u, y, z) space using the corresponding sinc functions after each ray is traced. While this image-domain formulation is conceptually simpler, it does not actually lead to any savings in computation time when compared to the frequency-aspect approach. Next we shall apply a fast ray summation scheme to speed up the calculation of (12).

B. Fast Ray Summation

Let us rewrite the image-domain ray summation formula as

$$\text{ASAR}(u, y, z) = \sum_{i\,\text{rays}} \beta_i \cdot h(u-u_i, y-y_i, z-z_i) \quad (13)$$

where $h(u, y, z)$ is the image-domain ray spread function given by

$$\begin{aligned}&h(u, y, z)\\ &\quad = e^{jk_ou}\,\text{sinc}(\Delta ku) \cdot \text{sinc}\,(k_o\Delta\phi y) \cdot \text{sinc}\,(k_o\Delta\theta z)\end{aligned} \quad (14)$$

and $\beta_i = (8k_o^2\Delta k\Delta\phi\Delta\theta) \cdot \alpha_i$. We now make an important observation that (13) can be recast into a convolution form between a 3-D weighted impulse function and the ray spread function as shown below

$$\begin{aligned}&\text{ASAR}(u, y, z)\\ &\quad = \left(\sum_{i\,\text{rays}} \beta_i \cdot \delta(u-u_i, y-y_i, z-z_i)\right) * h(u, y, z)\\ &\quad = g * h(u, y, z).\end{aligned} \quad (15)$$

To calculate the convolution, we will use an FFT-based fast scheme proposed earlier by Sullivan [11]. The basic idea is to use the FFT algorithm to carry out the convolution. However, since the 3-D weighted impulse train g in the above equation does not occur on a uniformly sampled grid, we must first convert it into a uniformly sampled one g_s. To ensure accuracy, we interpolate the nonuniformly sampled impulses onto a uniformly sampled grid which is sampled at N times the Nyquist rate. We use a first-order interpolation scheme, whereby the closest eight neighboring points on the uniform grid are linearly updated depending on their distances from the

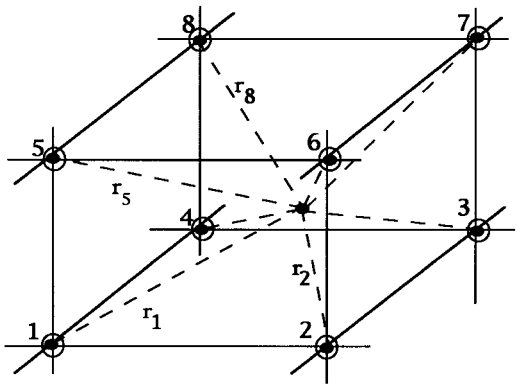

Fig. 8. The first-order, closest neighbor interpolation used in the Sullivan scheme.

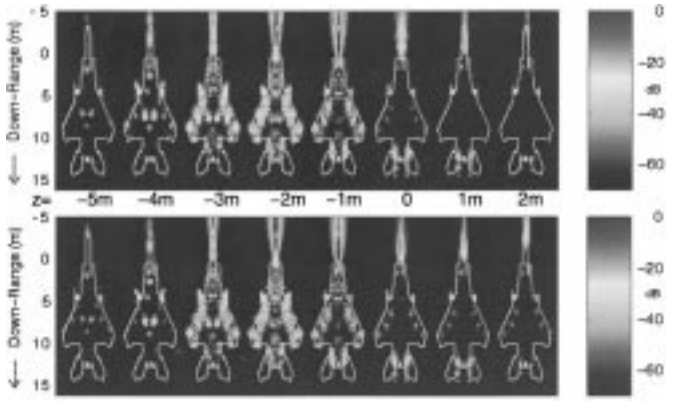

Fig. 9. Slice-by-slice comparison for the 3-D ASAR images at nose-on generated using the image-domain formulation with: (top) brute-force convolution and (bottom) Sullivan scheme.

original impulse (see Fig. 8). If the original impulse occurs between $j\Delta_u \le u_i < (j+1)\Delta_u$, $k\Delta_y \le y_i < (k+1)\Delta_y$, and $l\Delta_z \le z_i < (l+1)\Delta_z$ with an amplitude of α_i, the eight grid points are updated using a standard interpolation scheme [14] as follows:

$$\begin{aligned}
g_s(j\Delta_u, k\Delta_y, l\Delta_z) &= \alpha_i/(r_1 \cdot R)\\
g_s(j\Delta_u, k\Delta_y, (l+1)\Delta_z) &= \alpha_i/(r_5 \cdot r)\\
g_s((j+1)\Delta_u, k\Delta_y, l\Delta_z) &= \alpha_i/(r_2 \cdot R)\\
g_s((j+1)\Delta_u, k\Delta_y, (l+1)\Delta_z) &= \alpha_i/(r_6 \cdot R)\\
g_s((j+1)\Delta_u, (k+1)\Delta_y, l\Delta_z) &= \alpha_i/(r_3 \cdot R)\\
g_s((j+1)\Delta_u, (k+1)\Delta_y, (l+1)\Delta_z) &= \alpha_i/(r_7 \cdot R)\\
g_s(j\Delta_u, (k+1)\Delta_y, l\Delta_z) &= \alpha_i/(r_4 \cdot R)\\
g_s(j\Delta_u, (k+1)\Delta_y, (l+1)\Delta_z) &= \alpha_i/(r_8 \cdot R)
\end{aligned} \tag{16}$$

where

$$R = 1/r_1 + 1/r_2 + 1/r_3 + 1/r_4 + 1/r_5 + 1/r_6 + 1/r_7 + 1/r_8$$

and the r_i's are the distances from the eight grid points to the original impulse location as shown in Fig. 8. After summing all rays to form the uniformly sampled function g_s, the ASAR image can be generated by the fast Fourier transform

$$\begin{aligned}
&\mathrm{ASAR}(u, y, z)\\
&\quad = \mathrm{IFFT}_3\{\mathrm{FFT}_3(g_s(u, y, z)) \cdot \mathrm{FFT}_3(h(u, y, z))\}
\end{aligned} \tag{17}$$

where FFT_3 and IFFT_3 correspond to the 3-D forward and inverse fast Fourier transforms, respectively. The final u-to-x transformation is carried out just as in the frequency-aspect approach to generate ASAR (x, y, z). It is apparent that Sullivan's scheme can become more accurate by either increasing the oversampling rate N or using a higher order interpolation scheme. Accuracy, however, is achieved at the price of either more memory or more computation time. Detailed discussion on the computational complexity of the Sullivan scheme can be found in [12]. Finally, since we used a Hanning window prior to the FFT operation in the frequency-aspect approach, the h function in the fast algorithm can be simply obtained by inverse Fourier transforming the Hanning windows. We observe that the windowing operation used in the frequency-aspect approach can be easily implemented in the fast algorithm by replacing the $\mathrm{FFT}_3(h)$ by a 3-D Hanning window.

C. Results

The fidelity and computation time of the fast ASAR image-formation scheme are investigated. As a first example, the 3-D ASAR image presented in Fig. 6(b) is regenerated using the image-domain formulation, both with and without the fast ray summation scheme of Section III-B. Fig. 9 (top) shows the image-domain result by using a brute-force computation of the convolution in (12). Fig. 9 (bottom) shows the result using the fast ray summation technique. A visual comparison of Figs. 6(b), 9 (top), and 9(bottom) shows that the dominant scattering features are well reproduced in all three images over a dynamic range of 40 dB. The discrepancies between Figs. 6(b) and 9 (top) can be attributed to the approximation that the ray coefficient α_i is independent of aspect and frequency in the image-domain derivation. Some minor discrepancies in the strength of the scatterers are observed between Fig. 9 (top) and 9 (bottom), and are attributable to the Sullivan scheme. In implementing the Sullivan scheme, the oversampling ratio N is taken to be 4 in all three dimensions. As a second example, the 2-D projected ASAR image presented in Fig. 7 is regenerated using the image-domain formula. Fig. 10(a) shows the image-domain results by using the brute-force convolution. Fig. 10(b) shows the results using the fast ray summation technique. Again, we observe that the dominant scattering features are fairly well reproduced when the three images are compared. To demonstrate the computation time savings of the fast algorithm, we compare the computation time needed to form a single 3-D ASAR image using SBR for: 1) the frequency-aspect approach; 2) the image-domain approach with direct convolution; and 3) the image-domain approach with Sullivan's fast ray summation scheme. The timing results are listed in Table I, and have been broken down into the ray tracing time and the ray summation time. For the frequency-aspect approach and the image-domain with direct convolution approach, we observe that the ray summation time is the dominant portion of the whole image generation process. On the other hand, with the use of the

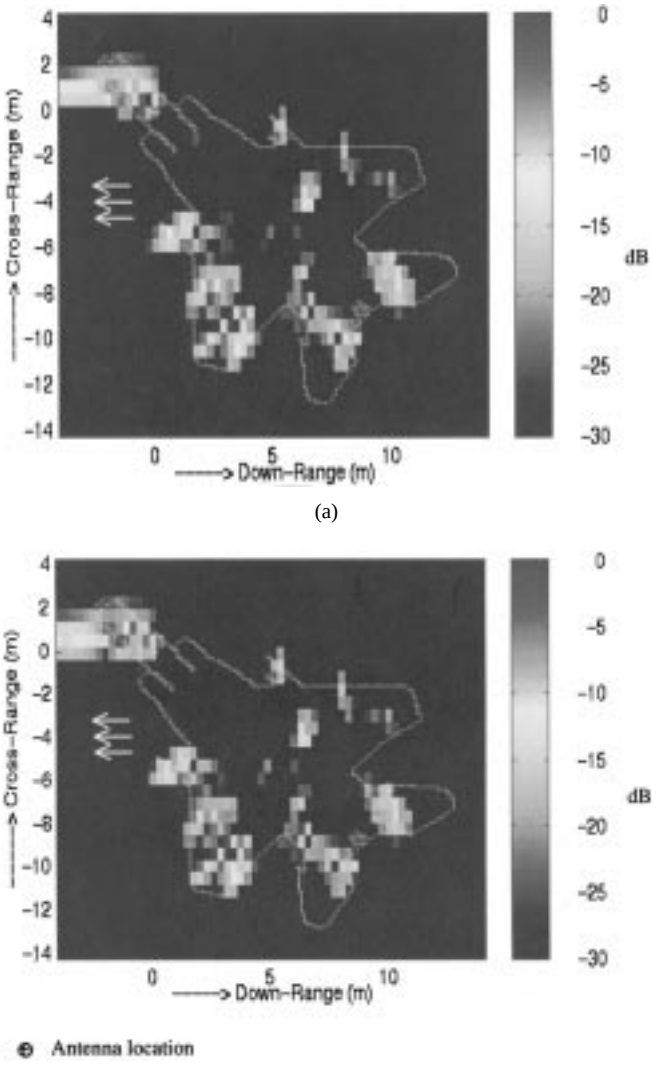

(a)

(b)

Fig. 10. Comparison of the 2-D ASR images at 45° from nose-on generated using the image-domain formulation with (a) brute-force convolution and (b) Sullivan scheme.

TABLE I
THE COMPUTATION TIMES FOR THE "v1old."
THE TIMINGS ARE FOR THE IBM(RS-6000/590) MACHINE

	Ray Summation Time	Ray Trace Time	Total Time
Frequency-Aspect Approach	79.25 hours	45 minutes	80 hours
Image Domain Approach	72.55 hours	45 minutes	73.3 hours
Sullivan's Scheme	3 minutes	45 minutes	48 minutes

image-domain approach accelerated by Sullivan scheme, the ray summation time can be reduced to 3 min from 80 h. The ray tracing time, of course, does not change in any of these approaches. Therefore, we have essentially reduced the ASAR image simulation time to simply ray tracing by using the fast algorithm.

IV. CONCLUSIONS

We have developed a novel imaging algorithm to pinpoint the locations of secondary scattering off a mounting platform from the antenna radiation data. Our approach is based on synthetic aperture radar concept. It was shown that under the small-angle approximation and single-bounce assumption, a Fourier transform relationship exists between multifrequency, multiaspect radiation data and the 3-D positions and strengths of the secondary scatterers on the platform. Therefore, a 3-D image showing the spatial locations of platform scattering can be constructed via Fourier inversion of the radiation data. We have demonstrated this concept by using the computed radiation data from a mounted antenna on a model airplane, simulated using the SBR-based code Apatch. By forming the 3-D image using the ASAR algorithm, the key scattering locations on the platform can be clearly identified. While the algorithm has only been demonstrated visually in the form of ASAR images in this paper, we have since verified that the strong scattering locations in the image can indeed be correlated with platform scattering [15]. For instance, by coating the platform at these key locations, we can significantly reduce the platform scattering. The ASAR algorithm is quite general in that it can be used to process data from any CEM solvers, or even measurement data. Work is currently under way to independently verify the ASAR concept using the fast-multipole solver FISC [16]. We have also derived a fast ASAR imaging algorithm specially tailored for the SBR approach. By taking advantage of the ray tracing information within the SBR engine, we have shown that the fast approach can result in the same quality of image as the frequency-aspect algorithm at only a fraction of the computation time (minute versus hour). Our work demonstrates that a fast computer-aided design tool that which combines antenna pattern simulation with scattering location diagnostic can be readily implemented. Such a tool should be useful in helping the antenna designer understand cause-and-effect and in guiding the designer to mitigate platform effects.

REFERENCES

[1] C. C. Lu and W. C. Chew, "A multilevel algorithm for solving boundary integral equation of scattering," *Microwave Opt. Technol. Lett.*, vol. 7, pp. 466–470, July 1994.
[2] J. M. Song and W. C. Chew, "Multilevel fast multipole algorithm for solving combined field integral equation of electromagnetic scattering," *Microwave Opt. Tech. Lett.*, vol. 10, pp. 14–19, Sept. 1995.
[3] H. Ling, R. Chou, and S. W. Lee, "Shooting and bouncing rays: Calculating the RCS of an arbitrary shaped cavity," *IEEE Trans. Antennas Propagat.*, vol. 37, pp. 194–205, Feb. 1989.
[4] J. Baldauf, S. W. Lee, L. Lin, S. K. Jeng, S. M. Scarborough, and C. L. Yu, "High frequency scattering from trihedral corner reflectors and other benchmark targets: SBR versus experiment," *IEEE Trans. Antennas Propagat.*, vol. 39, pp. 1345–1351, Sept. 1991.
[5] S. W. Lee, "Users manual for APATCH," DEMACO, Inc., Tech. Rep., Champaign, IL, Oct. 1992, version 1.
[6] T. Ozdemir, M. W. Nurnberger, J. L. Volakis, R. Kipp, and J. Berre, "A hybridization of finite-element and high-frequency methods for pattern prediction for antennas on aircraft structures," *IEEE Antennas Propagat. Mag.*, vol. 38, pp. 28–38, June 1996.
[7] J. C. Bennet, A. P. Anderson, P. A. McInnes, and A. J. T. Whitaker, "Microwave holographic metrology of large reflector antennas," *IEEE Trans. Antennas Propagat.*, vol. AP-24, pp. 295–303, 1976.

[8] Y. Rahmat-Samii, "Surface diagnosis of large reflector antennas using microwave holographic metrology—An iterative approach," *Radio Sci.*, vol. 13, pp. 1205–1217, Sept.–Oct. 1984.
[9] D. L. Mensa, *High Resolution Radar Imaging.* Dedham, MA: Artech House, 1981.
[10] R. Bhalla and H. Ling, "Image-domain ray-tube integration formula for the shooting and bouncing ray technique," *Radio Sci.*, vol. 30, pp. 1435–1444, Aug.–Sept. 1995.
[11] T. D. Sullivan, "A technique of convolving unequally spaced samples using fast Fourier transforms," Sandia National Labs., Tech. Rep. SAND89-0077, Jan. 1990.
[12] R. Bhalla and H. Ling, "A fast algorithm for signature prediction and image formation using the shooting and bouncing ray technique," *IEEE Trans. Antennas Propagat.*, vol. 43, pp. 727–731, July 1995.
[13] S. W. Lee, H. Ling, and R. Chou, "Ray tube integration in shooting and bouncing ray method," *Microwave Opt. Technol. Lett.*, vol. 1, pp. 286–289, Oct. 1988.
[14] R. M. Mersereau and A. V. Openheim, "Digital reconstruction of multidimensional signals from their projections," *Proc. IEEE*, vol. 62, pp. 1319–1338, Oct. 1974.
[15] C. Ozdemir, R. Bhalla, and H. Ling, "A radiation center representation of antenna radiation pattern on a complex platform," *IEEE Trans. Antennas Propagat.*, to be published.
[16] *User's Manual for FISC (Fast Illinois Solver Code)*. Center for Computational Electromagnetics, University of Illinois at Urbana-Champaign and DEMACO, Inc., Champaign, IL, Jan. 1997.

Caner Ozdemir (S'95–M'97), for a photograph and biography, see p. 1264 of the August 1997 issue of this TRANSACTIONS.

Rajan Bhalla was born in Ambala, India. He received the B.S. degree in electrical engineering from the India Institute of Technology, New Delhi, India, in 1991, and the M.S. and Ph.D. degrees in electrical engineering from the University of Texas at Austin in 1993 and 1996, respectively.

While in graduate school he held a Research Assistantship in the Electrical Engineering Research Laboratory. Since 1996, he has been working at the University of Texas at Austin as a Research Engineer. He has published over 30 articles and reports in refereed journals and proceedings. His main research interests include radar signature prediction, computational electromagnetic techniques, signal modeling, and wireless communication.

Luiz C. Trintinalia, for a photograph and biography, see p. 227 of the February 1997 issue of this TRANSACTIONS.

Hao Ling (S'83–M'86–SM'92), for a photograph and biography, see p. 227 of the February 1997 issue of this TRANSACTIONS.